Materials Characterization 133 (2017) 10–16

Contents lists available at ScienceDirect

Materials Characterization

journal homepage: www.elsevier.com/locate/matchar

Electron detection modes comparison for quantification of secondary phases of Inconel 686 weld metal

Émerson Mendonça Miná[a,*], Yuri Cruz da Silva[a,1], Marcelo Ferreira Motta[a,1], Hélio Cordeiro de Miranda[a,1], Jean Dille[b,2], Cleiton Carvalho Silva[a,1]

[a] Universidade Federal do Ceará, Department of Metallurgical and Materials Engineering, Fortaleza, Ceará, Brazil
[b] Université Libre de Bruxelles, 4MAT Department, Brussels, Belgium

ARTICLE INFO

Keywords:
Quantify
Secondary electron
Backscattered electron
Inconel 686
Microstructure

ABSTRACT

Quantitative analyses produce important information concerning the microstructural characteristics of materials, which are reflected in the main properties of the materials. The secondary and backscattered electron modes represent the two main techniques most used in scanning electron microscopy, to produce images and, consequently, realize a quantitative analysis. However, each technique has its advantages and problems. The present work proposed evaluate what is the best SEM technique to quantify secondary phases in a cladding of Inconel 686, which can be extended to the other classes of nickel based alloys rich in Mo. It was performed a quantitative analysis of several images to characterize the microstructure of Inconel 686 weld cladding. The images were obtained using three modes: secondary electron (SE), Z contrast backscattered electron (BSE) and topographic backscattered electron (BSE). The segmentation and quantify of secondary phases was performed by SVRNA software. The statistical results revealed differences between the techniques. The secondary electron mode included several artefacts that reduced the precision of the quantification study. The BSE modes are shown to be the best techniques for quantification.

1. Introduction

Nickel-based alloys are a special class of materials which combine great mechanical properties even at high temperature with an excellent corrosion resistance in several environments [1,2]. The high costs associated with these alloys limit their use to severe service conditions with high responsibility applications, and for this reason close control of the microstructure is essential to guarantee the integrity of components and equipment.

Usually, studies correlate the effect of secondary phases on the main properties of materials. The morphology, size, distribution and amount of secondary phase will reflect on the hardness, toughness and strength [3–5]. In addition, the secondary phase has a direct impact on the corrosion resistance [6]. Recent work have simulated the precipitation kinetics of secondary phases in nickel alloys due to their strong impact on the properties [7]. Reports about autogenous welding of precipitation-strengthened nickel-based alloys, reveal the importance of secondary phases in the hardness balance of the join, including the respective heat affected zone [8]. Recent studies has proposed new models to predict the weldability and castability of precipitation-strengthened nickel-base superalloys, taking account the formation of secondary phases, which cause seriously metallurgical problems in this manufacture processes [9–10]. In this context, quantitative analyses are shown to be an effective and powerful tool to correlate these phases with the properties of nickel-based alloys [11].

In the case of welding cladding, in general the secondary phases will nucleate during the non-equilibrium solidification due to the fast cooling frequently imposed by welding processes [12]. For claddings manufactured for aggressive corrosion environments, the amount of the secondary phases will reduce the corrosion resistance. These secondary phases are rich in elements that participate in corrosion resistance. Previous results shows that this formation will reduce the concentration of Cr, Mo and W around the region in which they have nucleated [13,14]. These phenomena will reduce the corrosion resistance in the area close to the phase boundary between the matrix and precipitate [13,14]. Thereby, for a high amount of secondary phases, the cladding

* Corresponding author at: Campus do Pici, Building 1080, Fortaleza, 60.455-760, Brazil.
E-mail addresses: emina@metalmat.ufc.br (É.M. Miná), marcelof@ufc.br (M.F. Motta), hmiranda@ufc.br (H.C. de Miranda), jdille@ulb.ac.be (J. Dille), cleiton@metalmat.ufc.br (C.C. Silva).
[1] Campus do Pici, Building 1080, Fortaleza 60.455-760, Brazil.
[2] CP194/3 avenue F.Roosevelt 50, Ixelles, Brussels 1050, Belgium.

http://dx.doi.org/10.1016/j.matchar.2017.09.014
Received 22 June 2017; Received in revised form 12 September 2017; Accepted 12 September 2017
Available online 14 September 2017
1044-5803/

will have more phase boundaries, which will probably increase the susceptibility to corrosion, according to interfaces studies that report a strong enrichment of Cr, Mo and W close to these interfaces [15,16]. Therefore, quantitative analysis is an important means to understand the corrosion resistance of claddings.

The quantification of phases can be performed using several techniques, where in most cases the size of the particles will limit the technique to be used. For example, the use of light microscopy applied to Ni-based alloys is adequate to observe some microstructural features such as grains, dendrite growth and until the presence of secondary phases [17]. However, when applied to quantitative analysis of secondary phases, this technique has been considerate not adequate due to lower resolution and to the poor resultant contrast. On the other hand, nanometric phases observed in aluminum alloys, for example, require transmission electron microscopy (TEM) or atomic force microscopy (AFM) [18]. In terms of quantitative analyses of the secondary phases observed in the weld microstructure of nickel-based alloys, scanning electron microscopy (SEM) has been shown a good option, because the particles have dimensions of some microns [19].

In SEM there are two main electron matter interactions, which produce different images: secondary electrons (SE) from inelastic scattering and backscattered electrons (BSE) produced by elastic scattering [20]. The first produce a topographical image of the microstructure, highlighting boundaries and any other features that show a kind of topography [20]. Thus, with the aid of specific etching, it is possible to highlight the secondary phase, allowing for easy quantification. The BSE technique, on the other hand, will separate the phases by chemical composition due to the elastic scattering of the electron incident beam in relationship with the specimen [20]. The emissivity of BSE is dependent on the atomic number of the elements that compounds the phases, these being large for elements with higher atomic numbers [5,20,21]. Thus, secondary phases that have a high content of elements such as Mo and W will show a different contrast when compared to the matrix [22]. However, each technique has its own particularity, with advantages and measurement errors that must be considered to conclude the analysis.

An indispensable step in quantification of secondary phases is the segmentation of images. This technique allows separate what is the object and the matrix. In this context, the SVRNA software has been pointed in previous work as a great accurate software for segmentation and quantification [23–26]. This software is based on a neural network that increases the precision in the segmentation and subsequent quantification.

Concerning the quantification of secondary phases in weld metal of nickel based alloys, several works has been reported, and in the most cases using secondary electrons mode in SEM [23,27,28]. Considering the potential of backscattering electrons in separate phases by atomic contrast, the present study proposes to evaluate the best SEM technique to perform a quantitative analysis of an Inconel 686 weld cladding by different modes of SEM operation, highlighting the difference between the use of secondary and backscattered electrons to execute the analysis. The expectation is obtain support to point the best of image acquisition mode, which can be extended to others Ni-Cr-Mo based alloys.

2. Experimental Methods

The study was performed on the cladding of a Ni-based alloy as a sample to obtain the images for the analysis. The cladding was manufactured by the GTAW process using a filler metal of ER Ni-Cr-Mo-14 (Inconel 686) deposited under ASTM A36 plate. The microstructure of the cladding was revealed using electrolytic etching with an aqueous solution of 10% chromic acid. A soft etching was applied in order to reduce the excessive corrosion of interdendritic regions.

To obtain the images a Quanta FEI 250 SEM was selected, using the modes: SE, Z contrast BSE and topographic BSE. For each technique evaluated, 100 images were produced. Each image was acquired from the same region when using all techniques, thus improving the comparison between the image acquisition modes. All images were taken using the same high tension, spot size and magnification. The contrast and brightness were kept constant for each technique according to their particularities.

The images were segmented to assist the quantification of secondary phases. The software adopted to perform the quantification was SVRNA, which is based on an artificial neural network. Previous studies revealed that SVRNA's performance in segmenting and quantifying the weld microstructure of nickel-based alloys was more precise than some commercial software [23]. In addition, SVRNA demonstrates a good performance in segmenting the microstructures of other materials [24–26].

For the techniques chosen, analysis was performed using the SE and BSE modes. In addition, another possibility of BSE detection was evaluated using a special detector, which collected the backscattered electrons that were returned from the sample at a slightly different angle from 180° in relationship with the incident electron beam. This system improved the quality of the images due to the large amount of backscattered electrons detected, thus allowing a Z contrast image with a special topographic contrast.

The statistical analysis was based on the ASTM A1245 standard. A 95% confidence interval was adopted [29]. Eq. (1) shows how to obtain the 95% CI. The σ represents the standard deviation of the measures and the coefficient t is known as the Student's t distribution, which depends on the population number (n). The ASTM A1245 standard recommends a t coefficient equal to 2 for a population number up to 30 measurements [29].

$$95\%\mathrm{CI} = \frac{t\sigma}{\sqrt{n}} \tag{1}$$

To conclude the statistical analysis, it is still necessary to evaluate the relative accuracy (RA). Thus, Eq. (2) takes the confidence interval calculated and realizes a comparison with the average measurements ($\overline{X}$), giving an estimation of the study error. According to the ASTM A1245 standard, for a $\%RA$ more than 30% it is necessary to acquire new fields to reduce the error [29].

$$\%RA = \frac{95\%\mathrm{CI}}{\overline{X}} \times 100 \tag{2}$$

The X-ray energy dispersive spectroscopy (EDS) analyses were performed on 30 particles of secondary phases to obtain the chemical composition. The same methodology was used in the interdendritic and dendrite regions. The results of the compositions were used to calculate the BSE contrast between the phases. All EDS analyses were performed using the FEI Quanta 450 FEG microscope, following the recommendations proposed by the ASTM E1508 standard, concerning the beam interaction with the matrix [30].

3. Results and Discussion

Fig. 1 shows micrographs obtained in a random region using the three techniques. In Fig. 1(a), (c) and (e) it is possible to see the original images obtained using the SE mode, Z contrast BSE mode and topographic BSE mode, respectively. Each technique highlighted the secondary phases using its particular physical principle. The segmented images observed in Fig. 1(b), (d) and (f) show a good correlation with the original images, thus demonstrating that the segmentation was performed very well by the SVRNA software.

The SE mode has the best resolution of all the techniques. This is due to a small emitted region, very close to the surface, from which the secondary electrons responsible for producing the image escape [20]. The SE images have good quality due to the large amount of electrons that are collected by the SE detector [31]. In addition, it is possible to see the topography, which was produced by selective etching, which allows the secondary phases to be highlighted. However, the SE

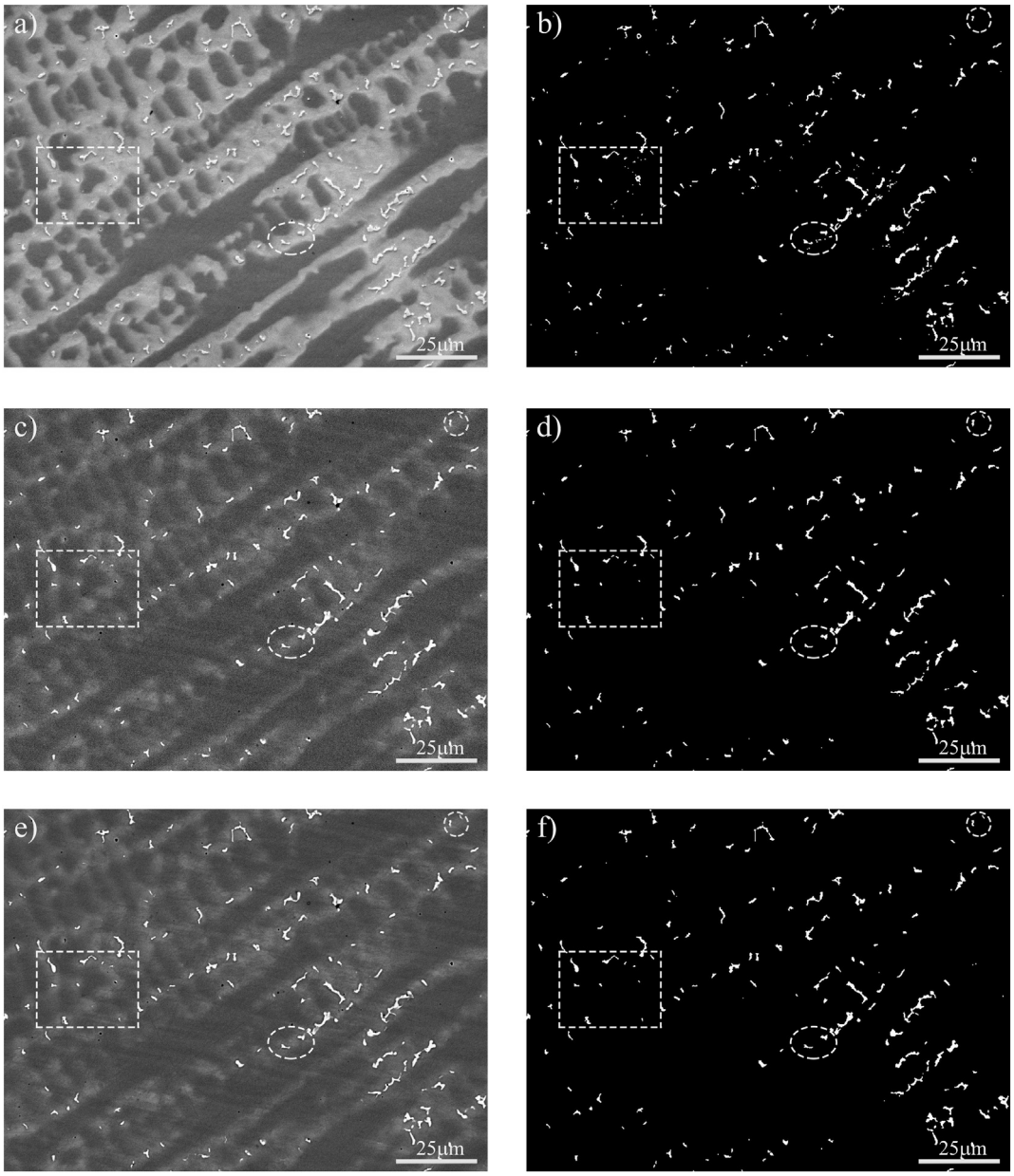

Fig. 1. Images obtained using the techniques a) SE, b) segmented SE image, c) Z contrast BSE, d) segmented Z contrast BSE image, e) topographic BSE and f) segmented topographic BSE image.

technique exposes some defects such as holes, which were probably generated by the detachment of inclusions during the polishing.

The Z contrast BSE image is shown in Fig. 1(c), which is of poorer quality than the other techniques. The noise observed in this image is a consequence of the smallest amount of electrons which return to the detector [31]. However, only backscattered electrons with high energy are collected. Thus, the result is a flat image with a compositional contrast, since elements with high atomic numbers will produce more backscattered electrons than low atomic number atoms [5,20,21]. The result is an image with a high contrast between the matrix and the secondary phases [5,20,21].

The topographic BSE shown in Fig. 1(e) is an image of slightly better quality than the image produced by the Z contrast BSE mode. Some backscattered electrons emitted by defects such as grain boundaries, which are normally lost due to the emitted angle being far from 180°, can be collected using this technique, thus improving the image quality by reducing the noise [31]. In addition, it is possible to observe a topographic image. As in the Z contrast BSE mode, the topographic BSE mode shows a compositional image with a better quality. In addition, it is possible to see topographic information.

The segmented images observed in Fig. 1(b), (d) and (f) show a similar result, with the many dispersed secondary phases highlighted in white. All of the techniques separated the secondary phases from the matrix very well. The secondary phase fractions in Fig. 1(b) (SE image), (d) (Z contrast BSE image) and (f) (topographic BSE image) were approximately 1.66%, 1.51% and 1.55%, respectively. Although all of the segmented images seem to be equal, they show small differences in their quantification.

The quantification of the SE image shows the highest value of all the techniques, followed by the topographic BSE and Z contrast BSE. The segmented images reveal that the SE mode has problems with the segmentation. For example, the circle highlights a secondary phase undetected in the SE segmented image because of the similarity of its grey tone with the grey tone of the matrix. The same phenomenon was observed in the ellipse highlighted, which includes the interdendritic region in the quantification due to the similar grey to that of the

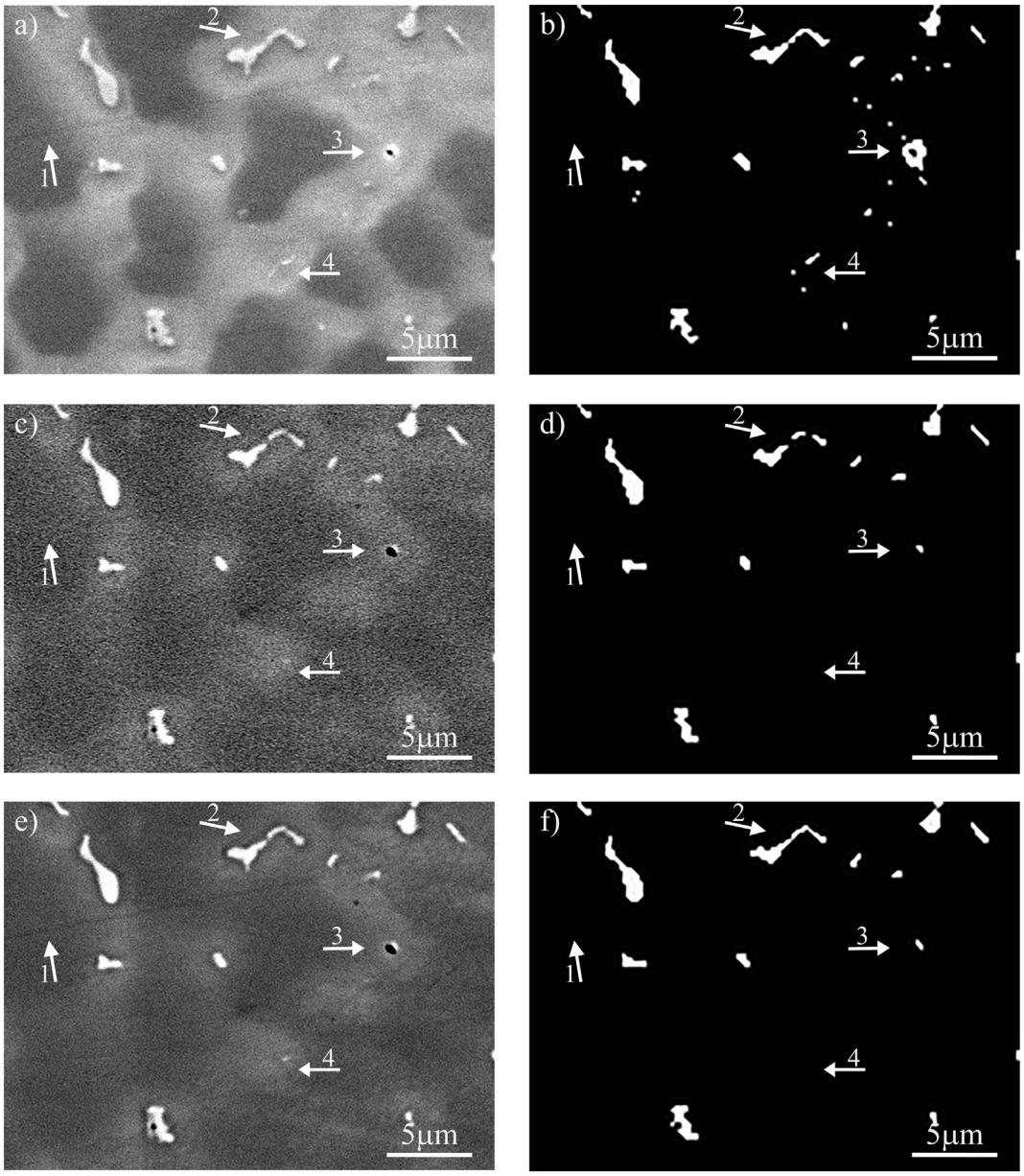

Fig. 2. Images obtained using the techniques a) SE, b) segmented SE image, c) Z contrast BSE, d) segmented Z contrast BSE image, e) topographic BSE and f) segmented topographic BSE image.

secondary phase. The final quantification result is the combination of small errors that sometimes include artefacts in the quantification as secondary phase, and sometimes does not include some of the secondary phase that has not been segmented very well.

Also concerning the previous quantitative results, it was found that BSE detection for both modes (topographic and Z contrast) show a similar result. The topographic BSE seems to be slightly bigger than the Z contrast BSE. This is probably due to the detection regions of some secondary phases that show a non-flat geometric form, which promotes the escape of BSE electrons at an angle slightly different from 180° in relationship with the incident beam.

Fig. 2 shows in detail the square highlighted in Fig. 1. The enlarged square reveals that the topographic BSE detected small scratches such as SE mode (arrows number 1), which denote the possibility of observing details about the topography. As previously discussed, the topographic BSE can detect some backscattered electrons that the Z contrast BSE mode cannot detect (arrows number 2). In addition, the segmented images reveal that the SE image highlighted artefacts and the interdendritic region, increasing errors in the analysis (arrows number 3). Besides this, a thin superficial secondary phase was observed in the SE image, but the same was not observed using the BSE techniques since the backscattered electrons are from a region below the surface. Thus, thin superficial microstructures are undetectable (arrows number 4). Comparing Fig. 3(d) and (f), it is possible to note that the topographic BSE seems to detect the thin secondary phases slightly better when compared to conventional BSE mode.

Fig. 3 shows in high magnification some microstructures, in order to understand the error produced when some artefacts that do not represent a secondary phase are included in the quantification. As previously discussed, the SE image (Fig. 3(a)) increases the artefacts in many ways. It is possible to note in the segmented SE image (Fig. 3(b)) that the holes boundaries are clearly detected by the software due to the intense contrast, as a consequence of the large amount of electrons emitted from this region, which are collected by the detector. This phenomenon is known in electron microscopy as the edge effect. Fig. 4(a) shows a schematic of the edge effect on the emission of

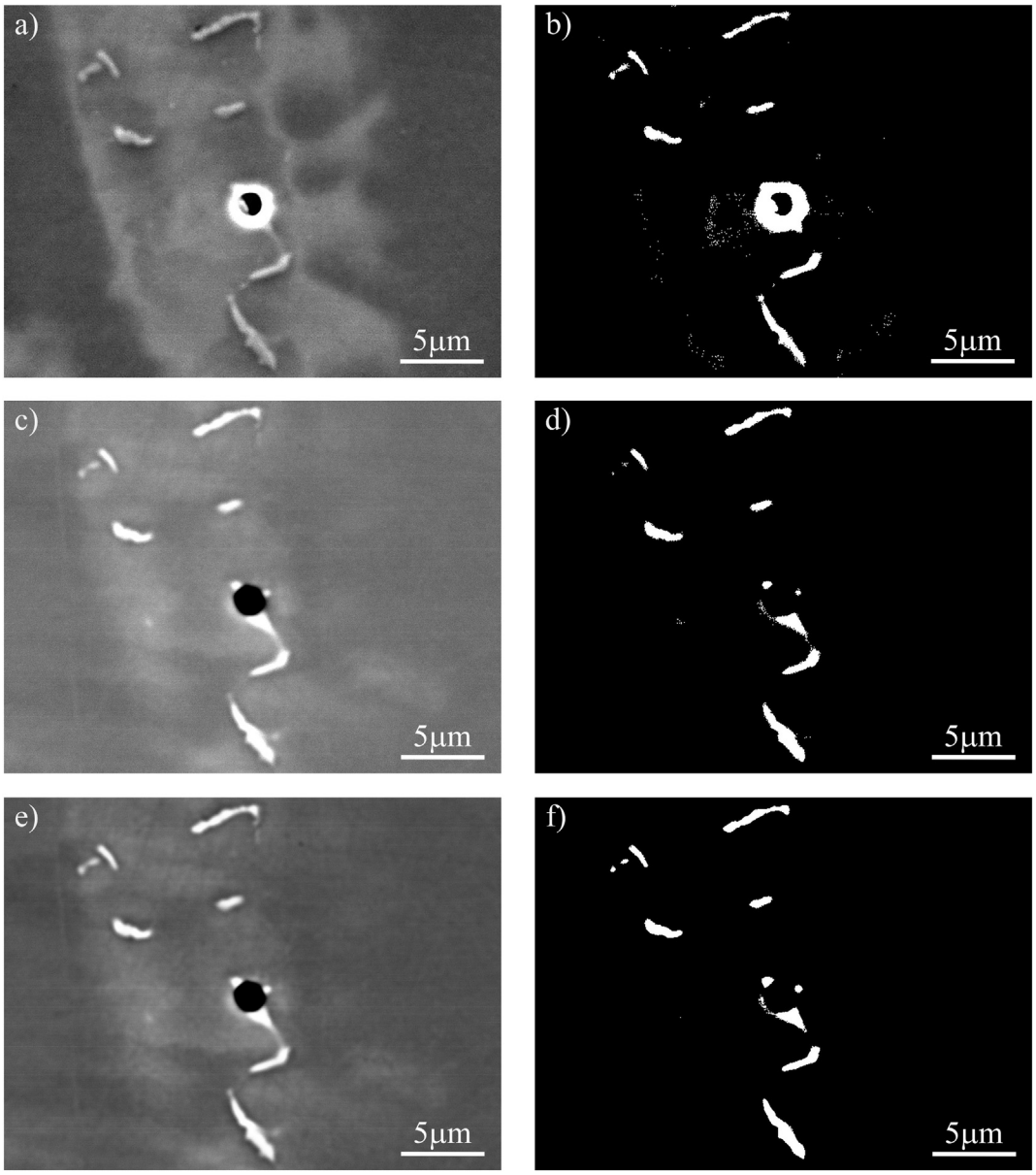

Fig. 3. A field in high magnification obtained using the techniques a) SE, b) segmented SE image, c) Z contrast BSE, d) segmented Z contrast BSE, e) topographic BSE and f) segmented topographic BSE image.

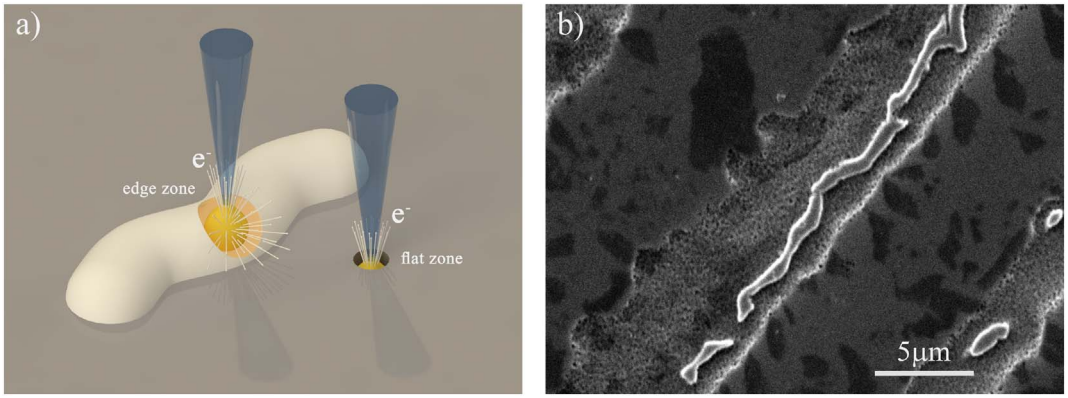

Fig. 4. The edge effect illustrated in a) schematic and b) microstructure. The microstructure was revealed by a severe etching. The arrows indicate the artefacts that impair the quantification analysis.

electrons, and illustrates the large amount of secondary electrons produced from the edges. Fig. 4(b) shows the microstructure of the same cladding, this time submitted to a severe etching, from which it is possible to note a strong brightness in the edges of the interdendritic region and in the edges of the secondary phases. In addition, this high production of secondary electrons in the edges promotes a different contrast, which turns the center of the precipitates to a grey tone similar to that of the matrix, thus impairing the quantification analysis.

Comparing Fig. 3(c), (d), (e) and (f), it is possible to note that the differences between the two BSE techniques are quite small. However, the better detection of topographic backscattered electrons provides the possibility of detecting small phases, in which the Z contrast BSE mode has difficulty. The secondary phase fractions obtained from Figs. 3(b), (d) and (f) had values of 2.23%, 1.41% and 1.44%, respectively. Note that there is a big difference in the percentage of secondary phases quantified by the SE image when compared to the Z contrast BSE. The difference found in this analysis was almost 58%. The same methodology for comparing the BSE techniques shows only a slight difference, approximately 2%.

The large amount of error associated with the quantification of the SE image is inherent in the use of the technique. The surface preparation by the mechanical polishing process and chemical or electrochemical etching introduces irregularities, which produce edge effects that make it difficult to perform the image quantification without including errors. The techniques using backscattered electrons have fewer problems with artefacts, because the contrast of each particle will depend strongly on the composition.

It is possible to estimate the influence of the elements/composition on the emissivity of BSE electrons by determining the BSE coefficient (η). Eq. (3) shows how the BSE intensity is calculated [5,21]. The equation of BSE intensity depends on the atomic number [5,21].

$$\eta = -0.0254 + 0.016Z - 1.86 \times 10^{-4} \times Z^2 + 8.3 \times 10^{-7} Z^3 \quad (3)$$

For complex phases composed of several elements, it is necessary to consider each one. Eq. (4) allows us to calculate the average backscattered coefficient of a specific phase considering the mass fraction c_i of each element [5,21].

$$\eta = \sum_i c_i \eta_i \quad (4)$$

With the backscattered coefficient of each phase, it is possible to check if the contrast between them will be enough to enable the software to separate the phases. Eq. (5) shows how to estimate the contrast [5,21].

$$C = \frac{\eta_\alpha - \eta_\beta}{\eta_\alpha}, \eta_\alpha > \eta_\beta \quad (5)$$

To estimate the BSE contrast, some EDS measurements of the secondary phases and the matrix were carried out, including the interdendritic and dendritic regions. Table 1 shows the average composition of the main phases observed in the microstructure. Applying the atomic numbers and the chemical compositions in Eqs. (3) and (4), it is possible to obtain the η BSE of individual elements and phases. Table 2 shows the η calculated for the present study.

Using the η phase coefficients calculated in Eq. (5), it is possible to obtain that the contrast of the dendrite and interdendritic regions in relationship with the secondary phases is approximately 8% and 7%, respectively. Therefore, based on the values obtained for this specific quantification study, the BSE techniques allow a contrast that is sufficient for quantification. It is important to highlight that many reports have reported on the influence of the matrix in EDS measurements due to the high beam interaction volume [32]. Studies revealed the stronger dependence of the interaction volume on the accelerating voltage and the chemical composition of the specimen [33,34]. In addition, according to the literature, the secondary phases observed in nickel-based alloys are known as topologically closed packages (TCP) [6,12–14,16,19]. These phases show a complex chemical stoichiometry, which can be tetragonal (σ-phase: $Cr_{0.99}Fe_{1.01}$) [35], rhombohedral (μ-phase: Co_6Mo_7) [36] and orthorhombic (P-phase: $Cr_9Mo_{21}Ni_{20}$) [37]. Thus, the chemical composition shown in Table 1 is the average of the sum of many possible secondary phases, including the effect of the matrix chemical composition.

Table 1
The chemical composition of main phases present in the microstructure obtained by EDS.

Microstructures	Chemical composition of phases (wt%)					
	Ni	Cr	Mo	W	Fe	Mn
Secondary phases	27.15	19.91	38.18	6.16	8.47	0.12
Interdendritic	47.82	19.73	16.72	3.46	12.01	0.26
Dendritic	52.10	18.23	12.28	4.04	13.19	0.15

Table 2
η BSE intensity of main elements and phases present in the microstructure.

Elements (η)	Ni	Cr	Mo	W	Fe	Mn
	0.29	0.26	0.38	0.48	0.28	0.27
Microstructures (η)	Secondary phase 0.33		Dendrite 0.30		Interdendritic 0.31	

Table 3 shows the statistical analyses of the secondary phase fraction obtained using each technique. As expected, the SE mode shows a higher secondary phase fraction average ($\overline{X}$) than the BSE techniques, followed by topographic BSE and Z contrast BSE. This difference is probably a consequence of the errors introduced. As previously discussed, the better quality of the topographic BSE images improves the detection of small phases, which the Z contrast BSE does not allow. Thus, the topographic BSE mode naturally provides a slightly better quantification.

A higher standard deviation (σ) was observed in measurements for all techniques. This was a consequence of heterogeneous microsegregation due to non-equilibrium solidification. As a result, in some fields an oscillating phase fraction was observed, from a small to a high amount, from one field to another. However, the relative accuracy of less than 5% shows that the number of measurements was satisfactory for this statistical study.

4. Conclusion

Based on the experimental results obtained in this study to compare the secondary electrons (SE) and backscattered electrons (BSE) techniques in quantifying the microstructure of Inconel 686 weld metal, it was possible to conclude that:

The SRVNA software demonstrates high accuracy in the segmentation and quantification of secondary phases, which allow compare the image acquisition modes using a scanning electron microscopy.

The SE mode shows a large amount of artefacts, increasing the measurement error, which were probably introduced by the surface preparation process, which includes polishing and etching, due to the edge effects.

The BSE modes offer the best image quality to quantify the area fraction of secondary phases. The choice between them will be defined

Table 3
Statistical quantification results.

	$\overline{X}$ (%)	σ	IC 95%	RA (%)
SE image	1.91	0.44	0.09	4.65
Z contrast BSE	1.77	0.39	0.08	4.40
Topographic BSE	1.84	0.40	0.08	4.31

by the image quality, considering the noise due to the small amount of BSE electrons collected. The BSE modes are found not to be influenced by artefacts, which increases confidence in the results compared to the SE mode.

Based on the comparison performed in this study it can be concluded that the BSE mode offers the best image quality to quantify secondary phases, and this knowledge can be extended for others nickel based alloys with high fraction of Mo and other elements commonly segregated such as W and Nb.

Acknowledgements

The authors would like to thank the Welding Research Technology Laboratory of the Universidade Federal do Ceará (UFC); The Analytical Center of the UFC, project 'CT-INFRA/MCTI-SISNANO/PRO' — EQUIPAMENTOS CAPES, for allowing the use of its electron scanning microscope for the analyses; and the agencies PETROBRAS (01.06.0172.06), FUNCAP (AE1-0079-000490100-13), CNPq, FINEP and CAPES (2929/13) for providing financial support to this study as well as undergraduate and Doctoral scholarships.

References

[1] T.M. Pollock, S. Tin, Nickel-based superalloys for advanced turbine engines: chemistry, microstructure and properties, J. Propuls. Power 22 (2006) 361–374, http://dx.doi.org/10.2514/1.18239.
[2] J.H. Perepezko, The hotter the engine, the better, Science 326 (2009) 1068–1069, http://dx.doi.org/10.1126/science.1179327.
[3] F. Masoumi, M. Jahazi, D. Shahriari, J. Cormier, Coarsening and dissolution of γ′ precipitates during solution treatment of AD730™ Ni-based superalloy: mechanisms and kinetics models, J. Alloys Compd. 658 (2016) 981–995, http://dx.doi.org/10.1016/j.jallcom.2015.11.002.
[4] J.-Y. Kang, S.-J. Park, D.-W. Suh, H.N. Han, Estimation of phase fraction in dual phase steel using microscopic characterizations and dilatometric analysis, Mater. Charact. 84 (2013) 205–215, http://dx.doi.org/10.1016/j.matchar.2013.08.002.
[5] G. Dimmler, P. Weinert, E. Kozeschnik, H. Cerjak, Quantification of the Laves phase in advanced 9–12% Cr steels using a standard SEM, Mater. Charact. 51 (2003) 341–352, http://dx.doi.org/10.1016/j.matchar.2004.02.003.
[6] M.J. Perricone, J.N. Dupont, Effect of composition on the solidification behavior of several Ni-Cr-Mo and Fe-Ni-Cr-Mo alloys, Metall. Mater. Trans. A 37 (2006) 1267–1280, http://dx.doi.org/10.1007/s11661-006-1078-7.
[7] F. Masoumi, D. Shahriari, M. Jahazi, J. Cormier, A. Devaux, Kinetics and mechanisms of γ' reprecipitation in a Ni-based superalloy, Sci. Rep. 6 (2016) 28650, http://dx.doi.org/10.1038/srep28650.
[8] Naffakh Moosavy, H., Aboutalebi, M.R, Seyedein, S.H., Mapelli, C. Microstructural, mechanical and weldability assessments of the dissimilar welds between γ′- and γ″-strengthened nickel-base superalloys, Mater. Charact., 82 (2013) 41–49. doi:http://dx.doi.org/10.1016/j.matchar.2013.04.018.
[9] H. Naffakh Moosavy, M.R. Aboutalebi, S.H. Seyedein, An analytical algorithm to predict weldability of precipitation-strengthened nickel-base superalloys, J. Mater. Process. Technol. 212 (2012) 2210–2218, http://dx.doi.org/10.1016/j.jmatprotec.2012.06.010.
[10] H. Naffakh Moosavy, M.R. Aboutalebi, S.H. Seyedein, C. Mapelli, A solidification model for prediction of castability in the precipitation-strengthened nickel-based superalloys, J. Mater. Process. Technol. 213 (2013) 1875–1884, http://dx.doi.org/10.1016/j.jmatprotec.2013.04.019.
[11] H. Zhao, B.P. Wynne, E.J. Palmiere, A phase quantification method based on EBSD data for a continuously cooled microalloyed steel, Mater. Charact. 123 (2017) 339–348, http://dx.doi.org/10.1016/j.matchar.2016.11.024.
[12] É.M. Miná, Y.C. da Silva, J. Dille, C.C. Silva, The effect of dilution on microsegregation in AWS ER NiCrMo-14 alloy welding claddings, Metall. Mater. Trans. A 47 (2016) 6138–6147, http://dx.doi.org/10.1007/s11661-016-3786-y.
[13] C.C. Silva, C.R.M. Afonso, A.J. Ramirez, M.F. Motta, H.C. Miranda, J.P. Farias, Assessment of microstructure of alloy Inconel 686 dissimilar weld claddings, J. Alloys Compd. 684 (2016) 628–642, http://dx.doi.org/10.1016/j.jallcom.2016.05.231.
[14] C.C. Silva, H.C.D. Miranda, M.F. Motta, J.P. Farias, C.R.M. Afonso, A.J. Ramirez, New insight on the solidification path of an alloy 625 weld overlay, J. Mater. Res. Technol. 2 (2013) 228–237, http://dx.doi.org/10.1016/j.jmrt.2013.02.008.
[15] B. Ge, Y. Luo, J. Li, J. Zhu, Study of γ/γ′ interfaces in nickel-based, single-crystal superalloys by scanning transmission electron microscopy, Metall. Mater. Trans. A 42 (2011) 548–552, http://dx.doi.org/10.1007/s11661-010-0566-y.
[16] C.C.A. Silva, C.R.M. Afonso, H.C. Miranda, A.J. Ramirez, Migração de Molibdênio na Interface Matriz/Precipitado em Metais de Solda de Ligas Ni-Cr-Mo, Technol. Metal. Mater. 8 (2011) 197–202, http://dx.doi.org/10.4322/tmm.2011.031.
[17] C. Yang, L. Liun, X. Zhao, Y. Li, J. Zhang, H. Fu, Dendrite morphology and evolution mechanism of nickel-based single crystal superalloys grown along the 〈001〉 and 〈011〉 orientations, Prog. Nat. Sci.: Mater. Int. 22 (2012) 407–413, http://dx.doi.org/10.1016/j.pnsc.2012.10.001.
[18] A.L. Garcia-Garcia, I. Dominguez-Lopez, L. Lopez-Jimenez, J.D.O. Barceinas-Sanchez, Comparative quantification and statistical analysis of η′ and η precipitates in aluminum alloy AA7075-T651 by TEM and AFM, Mater. Charact. 87 (2014) 116–124, http://dx.doi.org/10.1016/j.matchar.2013.11.007.
[19] É.M. Miná, Y.C.D. Silva, J. Dille, C.C. Silva, Efeito da Diluição Sobre a Microestrutura da Liga AWS ER NiCrMo-14 na Soldagem de Revestimentos pelo Processo TIG com Alimentação de Arame Frio, Rev. Soldag. Insp. 21 (2016) 317–329, http://dx.doi.org/10.1590/0104-9224/SI2103.07.
[20] J. Goldstein, D.E. Newbury, D.C. Joy, C.E. Lyman, P. Echlin, E. Lifshin, L. Sawyer, J.R. Michael, Scanning Electron Microscopy and X-ray Microanalysis, Third ed., Springer, US, 2003, http://dx.doi.org/10.1007/978-1-4615-0215-9.
[21] L. Korcakova, J. Hald, M.A.J. Somers, Quantification of Laves phase particle size in 9CrW steel, Mater. Charact. 47 (2001) 111–117, http://dx.doi.org/10.1016/S1044-5803(01)00159-0.
[22] J. Laigo, F. Christien, R. Le Gall, F. Tancret, J. Furtado, SEM, EDS, EPMA-WDS and EBSD characterization of carbides in HP type heat resistant alloys, Mater. Charact. 59 (2008) 1580–1586, http://dx.doi.org/10.1016/j.matchar.2008.02.001.
[23] V.H.C. De Albuquerque, C.C. Silva, T.I.S. Menezes, J.P. Farias, J.M.R.S. Tavares, Automatic evaluation of nickel alloy secondary phases from SEM images, Microsc. Res. Tech. 74 (2011) 36–46, http://dx.doi.org/10.1002/jemt.20870.
[24] V.H.C. De Albuquerque, J.M.R.S. Tavares, P.C. Cortez, Quantification of the microstructures of hypoeutectic white cast iron using mathematical morphology and an artificial neural network, Int. J. Microstruct. Mater. Prop. 5 (2010) 52–64, http://dx.doi.org/10.1504/IJMMP.2010.032501.
[25] V.H.C. De Albuquerque, P.P.R. Filho, T.S. Cavalcante, J.M.R.S. Tavares, New computational solution to quantify synthetic material porosity from optical microscopic images, J. Microsc. 240 (2010) 50–59, http://dx.doi.org/10.1111/j.1365-2818.2010.03384.x.
[26] V.H.C. De Albuquerque, P.C. Cortez, A.R. de Alexandria, J.M.R.S. Tavares, A new solution for automatic microstructures analysis from images based on a back-propagation artificial neural network, Nondestr. Test. Eval. 23 (2008) 273–283, http://dx.doi.org/10.1080/10589750802258986.
[27] S.G.K. Manikandan, D. Sivakumar, K. Prasad Rao, M. Kamaraj, Laves phase in alloy 718 fusion zone — microscopic and calorimetric studies, Mater. Charact. 100 (2015) 192–206, http://dx.doi.org/10.1016/j.matchar.2014.11.035.
[28] M. Anderson, A.-L. Thielin, F. Bridier, P. Bocher, J. Savoie, δ phase precipitation in Inconel 718 and associated mechanical properties, Mater. Sci. Eng. A 679 (2017) 48–55, http://dx.doi.org/10.1016/j.matchar.2014.11.035.
[29] Standard Practice for Determining the Inclusion or Second-Phase Constituent Content of Metals by Automatic Image Analysis, ASTM International, 2016. doi:http://dx.doi.org/10.1520/E1245-03R16.
[30] Standard Guide for Quantitative Analysis by Energy-Dispersive Spectroscopy, ASTM International, 2012. doi:http://dx.doi.org/10.1520/E1508-12A.
[31] M.T. Postek, A.E. Vladár, J.S. Villarrubia, A. Muto, Comparison of electron imaging modes for dimensional measurements in the scanning electron microscope, Microsc. Microanal. 22 (2016) 768–777, http://dx.doi.org/10.1017/S1431927616011430.
[32] J.E. Rossen, K.L. Scrivener, Optimization of SEM-EDS to determine the C–A–S–H composition in matured cement paste samples, Mater. Charact. 123 (2017) 294–306, http://dx.doi.org/10.1016/j.matchar.2016.11.041.
[33] T. Tokarski, G. Cios, A. Kula, P. Bała, High quality transmission Kikuchi diffraction analysis of deformed alloys — case study, Mater. Charact. 121 (2016) 231–236, http://dx.doi.org/10.1016/j.matchar.2016.10.013.
[34] P. Hovington, D. Drouin, R. Gauvin, CASINO: a new Monte Carlo code in C language for electron beam interaction — part I: description of the program, Scanning 19 (1997) 1–14, http://dx.doi.org/10.1002/sca.4950190101.
[35] H. Yakel, Atom distributions in sigma phases. I. Fe and Cr atom distributions in a binary sigma phase equilibrated at 1063, 1013 and 923 K, Acta Crystallogr. Sect. B: Struct. Crystallogr. Cryst. Chem. 39 (1983) 20–28, http://dx.doi.org/10.1107/S0108768183001974.
[36] J.B. Forsyth, L.M. d'Alte da Veiga, The structure of the [mu]-phase Co_7Mo_6, Acta Crystallogr. 15 (1962) 543–546, http://dx.doi.org/10.1107/S0365110X62001401.
[37] D.P. Shoemaker, C.B. Shoemaker, F.C. Wilson, The crystal structure of the P phase, Mo-Ni-Cr. II. Refinement of parameters and discussion of atomic coordination, Acta Crystallogr. 10 (1957) 1–14, http://dx.doi.org/10.1107/S0365110X57000018.